Scripta Materialia 222 (2023) 115049

Contents lists available at ScienceDirect

Scripta Materialia

journal homepage: www.journals.elsevier.com/scripta-materialia

# Crystallographic orientation-dependent deformation characteristics of additive manufactured interstitial-strengthened high entropy alloys

Wei Zhang [a], Jiajia Shen [c], J.P. Oliveira [c,d], Bart J. Kooi [b], Yutao Pei [a,*]

[a] Advanced Production Engineering, Engineering and Technology Institute Groningen, Faculty of Science and Engineering, University of Groningen, Nijenborgh 4, 9747 AG, the Netherlands
[b] Nanostructured Materials and Interfaces, Zernike Institute for Advanced Materials, Faculty of Science and Engineering, University of Groningen, Nijenborgh 4, 9747 AG, the Netherlands
[c] UNIDEMI, Department of Mechanical and Industrial Engineering, NOVA School Science and Technology, Universidade NOVA de Lisboa, Caparica 2829-516, Portugal
[d] CENIMAT/I3N, Department of Materials Science, NOVA School of Science and Technology, Universidade NOVA de Lisboa, 2829-516 Caparica, Portugal

ARTICLE INFO

*Keywords:*
Laser powder-bed fusion
High entropy alloy
Synchrotron X-ray diffraction
Crystallographic orientation
Micropillars

ABSTRACT

In this study, laser powder bed fusion (LPBF) was used for the fabrication of an interstitial-strengthened high entropy alloy (iHEA), $Fe_{49.5}Mn_{30}Co_{10}Cr_{10}C_{0.5}$ (at.%). The as-fabricated iHEA possesses excellent strength-ductility synergy during tensile loading, with fracture strength reaching up to 1109 MPa at 37% engineering strain. Electron backscatter diffraction (EBSD) and high energy synchrotron X-ray diffraction were used to evaluate the microstructural characteristics of the material. In-situ EBSD analysis during uniaxial tensile testing was performed to unveil the deformation mechanisms. Moreover, crystallographic orientation-specific micropillar compression tests were conducted to determine how the grain deformation characteristics differ between orientations. Due to the activation of multiple slip systems and the homogeneous plastic flow, the [111] orientation demonstrated a higher yield strength and continuous work hardening rate. This research helps in clarifying grain orientation-specific contributions to the bulk mechanical response of additively manufactured HEA.

The concept of high entropy alloys (HEAs) was first proposed in 2004 and has received extensive attention from academia since [1,2]. The near-infinite compositional space of HEAs offers the same near-infinite possibilities. To date, HEAs with high thermal stability, excellent corrosion resistance, high electrical resistivity, and good mechanical properties over a wide temperature range have been reported, showing broad application prospects in the aerospace, automotive and energy industries [3–6]. In recent years, to achieve superior strength-ductility synergy, interstitial-strengthened HEAs (iHEAs) have been developed to overcome the limitations of single-phase HEAs [7–10], among which the $Fe_{49.5}Mn_{30}Co_{10}Cr_{10}C_{0.5}$ (at.%) alloy shows very promising properties that can be tuned over a wide range of thermo-mechanical processing parameters. Its excellent mechanical properties benefit from the assistance of transformation-induced plasticity (TRIP) and/or twinning-induced plasticity (TWIP) effects, inspired by the strengthening and deformation mechanisms of several alloys with low stacking fault energy (SFE), such as high-manganese steels [11]. Additionally, the addition of carbon can promote interstitial solid solution strengthening as way to further increase the strength of iHEAs [12]. It is worth noting that most of the iHEAs are fabricated by casting with subsequent cold deformation and heat treatment [13], which may not be suitable for complex geometries required in industrial applications.

Laser powder bed fusion (LPBF), as a commonly used additive manufacturing (AM) method, allows the fabrication of complex-shaped parts layer-by-layer with high dimensional accuracy [14]. Moreover, due to its highly localized melting and solidification, this AM process generates unique microstructures different from conventional metallurgical routes [15]. The obtained microstructures often have obvious preferred orientations resulting from the high temperature gradient and extremely high cooling rate, which can be tuned by adjusting process parameters and scanning strategies [16]. On the other hand, since grains with different orientations have different deformation mechanisms under loading [17], understanding their orientation-specific mechanical properties can also provide new insights for the properties optimization of additively manufactured materials.

Currently, there are scarce reports on the LPBF of

* Corresponding author.
*E-mail address:* y.pei@rug.nl (Y. Pei).

https://doi.org/10.1016/j.scriptamat.2022.115049
Received 27 July 2022; Received in revised form 7 September 2022; Accepted 10 September 2022
Available online 15 September 2022

$Fe_{49.5}Mn_{30}Cr_{10}Co_{10}C_{0.5}$ iHEA [18], especially in what concerns the strengthening effect of interstitial carbon atoms, as well as the relationship between mechanical properties and grain structures, which must be revealed to further advance the understanding of these novel alloys. In the present study, the microstructure and deformation mechanisms of $Fe_{49.5}Mn_{30}Cr_{10}Co_{10}C_{0.5}$ iHEA fabricated by LPBF were analyzed by coupling electron backscatter diffraction, high energy synchrotron X-ray diffraction and mechanical property testing. Considering the effect of laser processing on tailoring the crystallographic orientations, the microscale mechanical behavior of the fabricated iHEA was evaluated by micropillar tests to better understand the dynamic strengthening mechanism and grain orientation interactions during external loading.

Gas-atomized pre-alloyed $Fe_{49.5}Mn_{30}Co_{10}Cr_{10}C_{0.5}$ (at.%) powders with diameters ranging from 15 to 53 μm were used as the feedstock material. The LPBF process was carried out using a SLM125 HL printer. A chessboard scanning strategy with 33° rotation between two consecutive layers was utilized, with the following laser processing parameters: laser power 300 W, scanning speed 700 mm/s, layer thickness 30 μm and hatch spacing 120 μm. The microstructure of the as-fabricated iHEA specimens was characterized by scanning electron microscopy (SEM, Tescan LYRA SEM-FIB) equipped with electron backscatter diffraction (EBSD) detector. Synchrotron X-ray diffraction experiment was performed at the P07B High Energy Beamline of PETRA III/DEST for phase identification. The applied wavelength was 0.14235 Å and the sample-to-detector distance was set to 1176 mm. The raw diffraction data was processed with Fit2D and MAUD. The phase fractions were calculated by the Rietveld refinement procedure. In this procedure, a six-degree polynomial function was used to reproduce the pattern background, while the Cagliotti PV model was selected for instrumental broadening and the Popa model was selected for anisotropic broadening. Besides, the extended Williams-Imhof-Matthies-Vinel algorithm (E-WIMV) [19] was used as the texture model, considering the texture evolution generated from the LPBF process. Moreover, $LaB_6$ calibrant powder was used to estimate the instrumental peak boarding associated with the beamline.

Tensile specimens with a gauge geometry of 11 (length) × 3 (width) × 1.2 (thickness) $mm^3$ were extracted by electrical discharge machining. Uniaxial tensile tests were conducted using a Kammrath & Weiss tensile module at a strain rate of $3 \times 10^{-4}$ /s at room temperature. In-situ EBSD analysis during tensile deformation was performed on the gauge plane to better understand the grain orientation-dependent deformation process. Micropillar compression testing was used to evaluate the micromechanical properties of the additively manufactured iHEA in three different crystallographic orientations close to [100], [110] and [111]. Micropillars with a diameter of 2 μm and a length of 6–7 μm were fabricated using focused ion beam (FIB), with a tapering effect limited to within 3°. The micropillars were compressed using an ASMEC nanotester (Dresden, Germany) equipped with a diamond probe of 5 μm diameter flat tip. The compression tests were performed in the displacement-control mode with a loading rate of 3 nm/s. In order to minimize the possible effect of grain rotation during deformation on the test results [20], the compression degree was limited to a 20% strain range.

Fig. 1 shows detailed results of the EBSD and SEM analysis on the as-fabricated iHEA. The 3D inverse pole figure (IPF) and corresponding phase maps are depicted in Fig. 1a and b, respectively, revealing the formation of coarse columnar grains, as well as few fine equiaxed grains along the laser scan tracks. Fig. 1c shows the internal boundaries and sub-grain structures of the as-fabricated iHEA. The fusion boundaries are aligned perpendicular to the build direction (Z), and the grain boundaries (GBs) are mostly aligned along the Z direction, forming columnar grains. In particular, within individual grains, cellular-like structures with honeycomb or dendritic morphologies with respect to the solidification direction can be clearly observed. This hierarchical heterogeneous microstructure is commonly reported in LPBF processed alloys [15,21,22], which contributes to typically observed superior mechanical properties. Generally, the grain structure formed during solidification of a specific alloy is governed by the degree of constitutional undercooling, that is, the ratio of the temperature gradient G to the solidification rate R (G/R). A high G/R ratio generally favors the formation of columnar grains, while a low G/R ratio promotes the formation of equiaxed grains [23]. The G value generated in the laser-based AM process is usually large (e.g. 207 K/mm for CoCrFeMnNi [24]), resulting in a larger G/R ratio, thus inhibiting the formation of massive equiaxed grains. The formation of a small number of fine equiaxed grains is mainly due to the

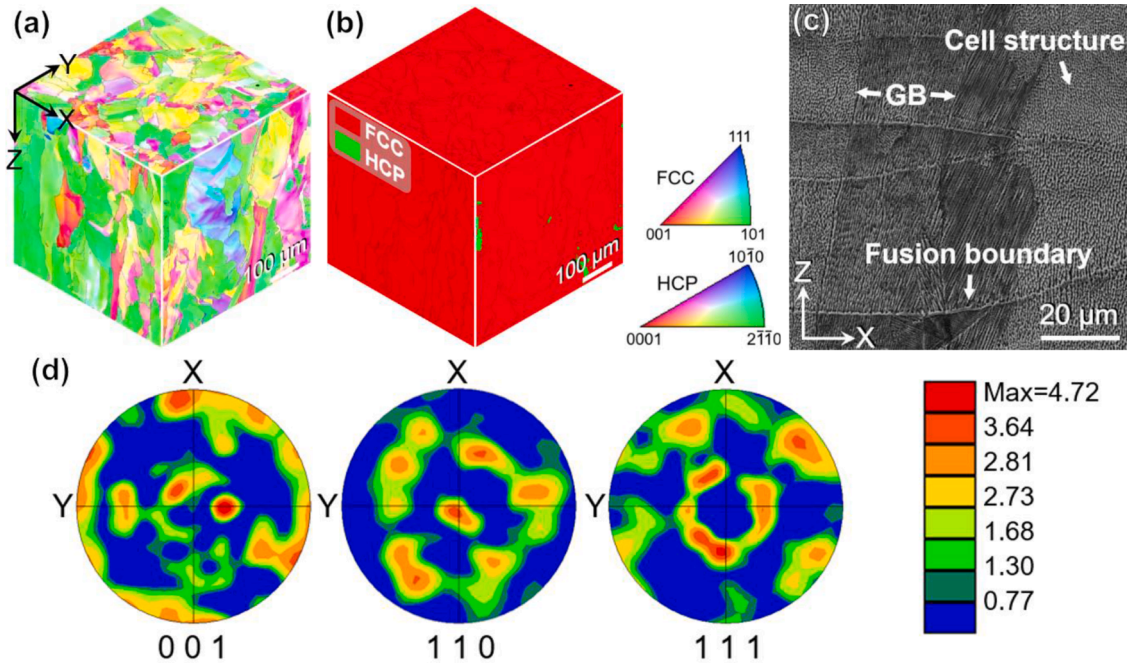


**Fig. 1.** (a) 3D-IPF map of the as-fabricated iHEA (IPF//Z), (b) corresponding phase map, (c) SEM micrograph of the as-fabricated iHEA, (d) pole figure from the XY plane.

lower constitutional undercooling (G/R) at the centerline of the adjacent laser scanning path. Furthermore, the high cooling rate ($10^6$ to $10^8$ K/s) of the LPBF process can effectively generate cylindrical cells with honeycomb-shaped cross-sections growing along the temperature gradient direction from the fusion boundaries [21,22]. Therefore, when considering the 3D structure of a cell, the morphology varies depending on the observation plane.

As can be seen from the phase maps in Fig. 1b, the majority of the microstructure has the fcc phase with a small amount (1.3 vol.%) of hcp phase interspersed. For metastable alloys with very low SFE, fcc and hcp are the stable phases at high temperature and low temperature, respectively [25]. Due to the extremely fast cooling rate of the LPBF process, the formation of the low-temperature hcp phase is almost fully suppressed, while the metastable fcc phase can be retained until room temperature under the non-equilibrium solidification conditions experienced by the material [26]. The harmonic texture of the pole figure (PF) is shown in Fig. 1d, where a relatively concentrated (110) crystallographic orientation parallel to the build direction is observed due to the applied scanning strategy, similar to that in [16].

High energy synchrotron X-ray diffraction was performed on the gauge plane to accurately analyze the existing phases, as shown in Fig. 2. Diffraction peaks corresponding to both the fcc and hcp phases are observed. The low-intensity diffraction peaks of the hcp phase are detailed in the insert of Fig. 2, with a volume fraction of 2.29%, as calculated by Rietveld refinement. In addition, $M_{23}C_6$ and $M_7C_3$ carbides with volume fraction of 1.85% and 0.75%, respectively, were detected, while the former was also observed in additively manufactured C-containing CoCrFeNi HEAs [27, 28]. Such nano-scale carbides are usually distributed at grain boundaries and cell boundaries with dislocation pile-ups, which are beneficial to the strength enhancement [29].

Fig. 3a depicts the tensile stress/strain curve of the LPBF-fabricated iHEA, with the corresponding yield strength (YS), ultimate tensile strength (UTS), and fracture elongation indicated. The present iHEA exhibits an exceptional enhanced strength-ductility combination. The insert demonstrates a substantial and stable work hardening behavior, thereby favoring excellent macroscopic plasticity before complete fracture. Fig. 3b shows that the present alloy exhibits higher strength and/or greater elongation compared with other additively manufactured iHEAs [18,27,28,30-39], overcoming the strength-ductility trade-off.

To understand the origin of the excellent mechanical properties of the current additively manufactured iHEA, EBSD analysis at the same location on the gauge plane of tensile samples subjected to different degrees of engineering strain was performed, as shown in Fig. 3c. With increasing strain, a gradually increasing stripe-like hcp phase was observed inside the metastable fcc matrix, indicating that the fcc-hcp martensitic transformation occurred during plastic deformation, analogous to the TRIP mechanism in low SFE alloys [25, 40, 41]. The mechanical-induced martensitic transformation generates new dislocations and thus increases the dislocation density, and the hcp phase also acts as a secondary hardening mechanism due to the lack of plasticity of its crystal structure, so fcc-hcp martensitic transformation significantly contributes to the enhanced work hardening behavior and superior properties [25,40,41]. Furthermore, the abovementioned nano-scale $M_{23}C_6/M_7C_6$ carbides distributed at the grain and cell boundaries can effectively hinder the dislocation movement and generate high back stress through a large number of geometrically necessary dislocations (GNDs) during plastic deformation, further improving the alloy's strength [27,29]. Specifically, GNDs would be generated during plastic deformation to maintain physical continuity at the interfaces. In the materials with heterostructures, the GNDs can evolve more actively at the interface between hard and soft domains [29,42,43]. For the current LPBF-processed iHEA, since the carbides are significalty stronger than the soft FCC matrix, the FCC matrix would sustain higher plastic strain during plastic deformation, resulting in a localized strain gradient near the interface between the matrix and carbides. GNDs are then generated and piled up at the interface to accommodate the strain gradient, producing back stress induced hardening, which could be regarded as a key factor for the enhanced stress levels and strain hardening ability of LPBF-processed materials [29,31,32]. On the other hand, nano-carbides have been reported to have a stronger effect on blocking dislocation motion than cell boundaries [29], suggesting that the volume fraction of carbides may be an important factor for regulating the mechanical properties of LPBF-processed C-containing HEAs.

From the EBSD results in Fig. 3c, it can be noticed that at 5% strain, the hcp phase transformation occurs mainly in grains with specific orientations, such as grains with a ⟨112⟩ orientation parallel to the tensile direction (marked with ® in Fig. 3c). It is generally believed that the orientation of fcc grains affects the martensitic transformation behavior in steels [17]. Considering that additively manufactured materials usually have pronounced preferred orientations, it is of interest to investigate the effect of grain orientation on the deformation mechanisms. Therefore, micropillar compression experiments were performed on single grains with different orientations ([100], [110], [111]) parallel to the compression direction, and the results are shown in Fig. 4.

As can be seen from the compressive stress-strain curves shown in Fig. 4a, the elastic deformation stage is followed by micro-yielding with the occurrence of burst behavior for all micropillars. Compared with the [110] and [111] micropillars, the [100] micropillar exhibits significantly reduced yield strength, but work hardening can still be clearly observed. The [111] orientation, favorable for dislocation slip via activating multiple slip systems, shows a continuous work hardening with very small strain bursts, resulting in excellent mechanical properties. By contrast, the [110] micropillar exhibits a gradual decrease in flow stress after yielding. This substantial softening is thought fully attributed to that dislocation slip along the fcc/hcp phase boundaries becomes the dominant deformation mechanism instead of slip transfer across the phase boundaries, since the fcc and hcp phases have a $\langle 110\rangle_{fcc}//\langle 11\text{–}20\rangle_{hcp}$ orientation relationship [44], resulting in lower stress required to active partial migration and subsequent softening. Similar softening behavior has also been reported in nanotwinned metals [45]. Furthermore, the observed large strain bursts are also believed to be the result of strain softening, induced by dislocation slip or martensitic transformation [46]. Combined with the EBSD results in Fig. 3c, it could be assumed that the strain bursts in the micropillars are closely related to the martensitic transformation behavior during the compression tests. The [111] micropillar shows higher activation stress (yield strength) compared with that of the micropillars with [100] and [110] orientations. Under uniaxial loading of [100], [110] and [111] orientations, the corresponding Schmid factor of dislocation slip is the largest in the [100] orientation and the smallest in the [111] direction [47], which is

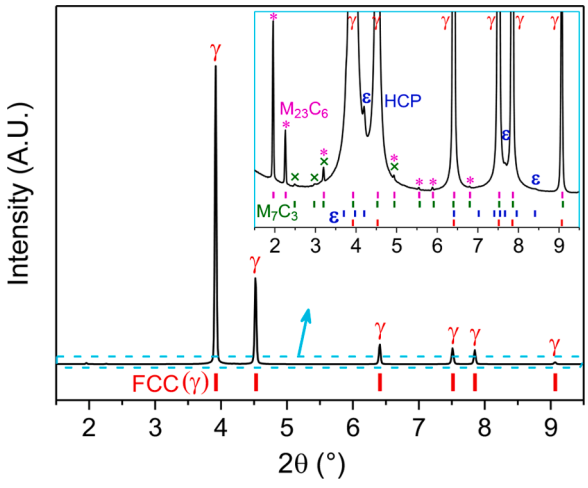


**Fig. 2.** Representative high energy synchrotron X-ray diffraction pattern of as-fabricated iHEA. The insert highlights the presence of hcp phase and carbide precipitates.

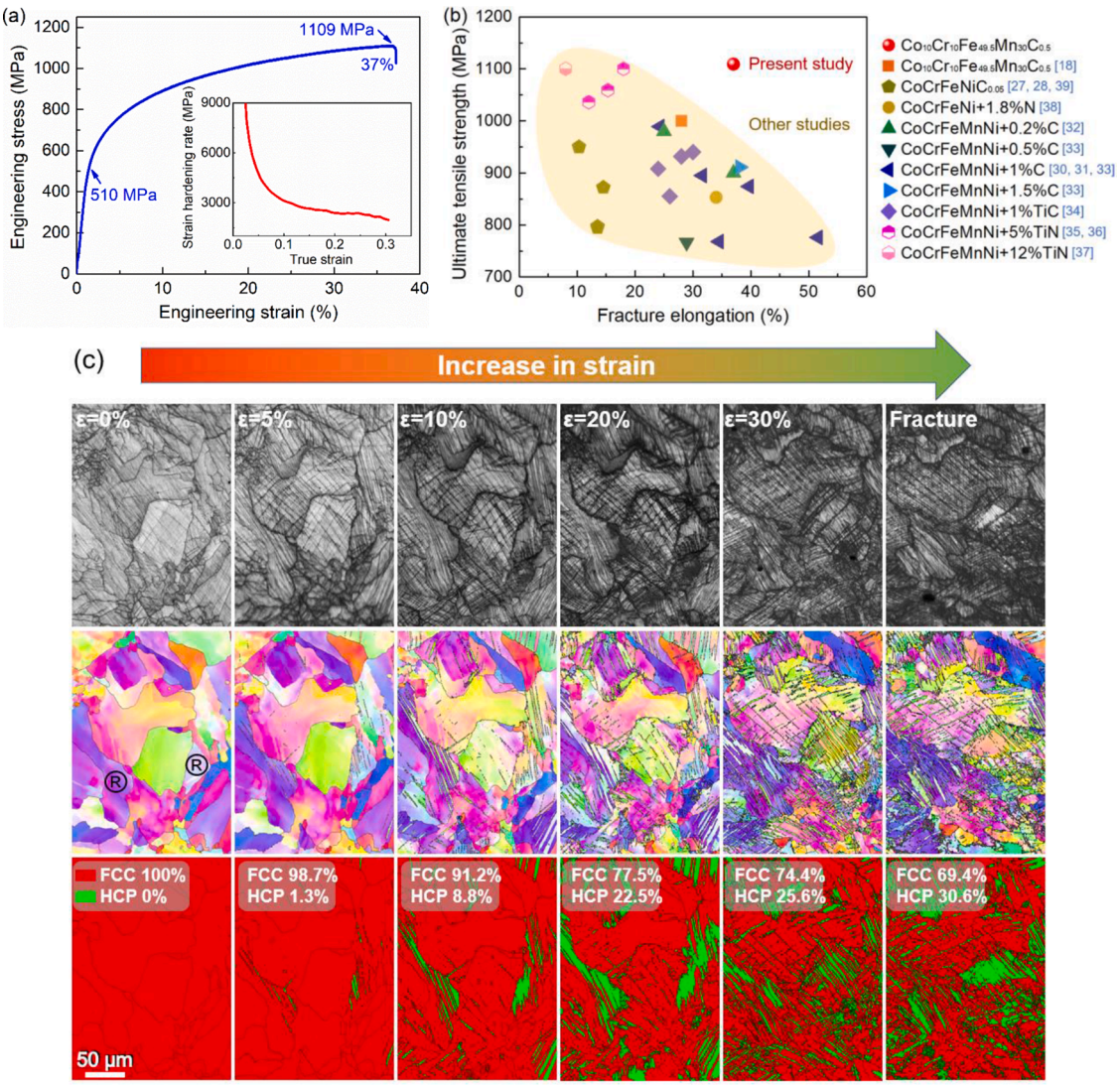


**Fig. 3.** (a) Engineering stress/strain curve of the LPBF-fabricated iHEA, the insert shows the strain hardening rate curve. (b) The strength/elongation of the present alloy compared with iHEAs fabricated by LPBF in other studies [18,27,28,30-39]. (c) In-situ EBSD analysis at different engineering strains.

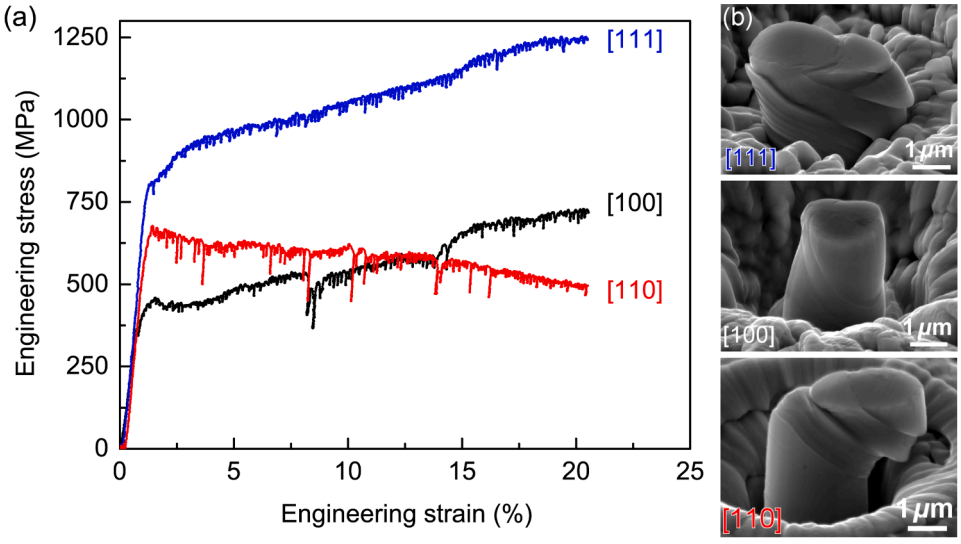


**Fig. 4.** (a) Engineering stress/strain curves of micropillars with different orientations. (b) SEM images of micropillar morphology after compression tests.

consistent with the activation stress observed in this study. In another report related to the orientation-dependent martensitic transformation mechanisms [17], it was found that in medium manganese steels, the average critical stress for martensitic transformation in [110] micropillars is significantly larger than that in [100] micropillars, which is attributed to the different martensitic transformation mechanisms. Namely, free-standing martensitic transformation for [110] micropillars and twin-assisted martensitic transformation for [100] micropillars. Compared with the former, lower activation stress is required for twin-assisted martensitic transformation as martensite nucleates at the intersection of deformation twin bundles, while [110] micropillars could nucleate from existing martensitic embryos.

Representative SEM images of the deformed micropillars in different orientations are shown in Fig. 4b. Straight shear slip traces are clearly observed in all micropillars, which mainly occur in the normal direction under the applied stress. Due to the activation of multiple slip systems, the deformed [111] micropillar surface shows slip traces in multiple directions. This type of deformation allows the micropillar to accommodate a large amount of strain without collapsing, as indicated by the stress-strain curve in Fig. 4a. Irregular surface traces are observed on the [100] micropillar, showing a "barrel" shape, which appears to be an internal expansion process. This surface morphology is commonly reported in fcc micropillars, where a heterogeneous martensitic transformation occurs during compressive tests [48]. By contrast, the surface morphology of the [110] micropillar exhibits deformation localization in several slip bands along the micropillar, and the deformation direction is gradually shifted from the normal direction of loading, leading to a certain degree of strain softening.

To sum up, the LPBF-fabricated $Fe_{49.5}Mn_{30}Co_{10}Cr_{10}C_{0.5}$ iHEA exhibits an exceptionally enhanced synergy of tensile strength (1109 MPa) and elongation (37%), which is mainly attributed to the fcc-hcp martensitic transformation deformation mechanism and strengthening effect of nano-carbides. The effect of crystallographic orientations on the critical stress for martensitic transformation as well as the work hardening behavior in LPBFed iHEA was revealed via micropillar compression tests. This study sheds light on the fundamental understanding of the contribution of grain orientation to the overall mechanical response of additive manufactured iHEA, helping to fabricate stronger and tougher engineering materials through additive manufacturing.

## Declaration of Competing Interest

The authors declare that they have no known competing financial interests or personal relationships that could have appeared to influence the work reported in this paper.

## Acknowledgment

WZ acknowledges the China Scholarship Council for funding the Ph. D. grant (CSC no. 201906250212). JPO and JS acknowledge Fundação para a Ciência e a Tecnologia (FCT - MCTES) for its financial support via the project UID/00667/2020 (UNIDEMI). JPO acknowledges the funding of CENIMAT/i3N by national funds through the FCT-Fundação para a Ciência e a Tecnologia, I.P., within the scope of Multiannual Financing of R&D Units, reference UIDB/50025/2020-2023. JS acknowledges the China Scholarship Council for funding the Ph.D. grant (CSC no. 201808320394). The authors acknowledge DESY (Hamburg, Germany), a member of the Helmholtz Association HGF, for the provision of experimental facilities. Beamtime was allocated for proposal I-20210899 EC. The research leading to this result has been supported by the project CALIPSOplus under the Grant Agreement 730872 from the EU Framework Programme for Research and Innovation HORIZON 2020.

## References

[1] J.W. Yeh, S.K. Chen, S.J. Lin, et al., Adv. Eng. Mater. 6 (2004) 299–303.
[2] B. Cantor, I.T.H. Chang, P. Knight, et al., Mater. Sci. Eng. A 375-377 (2004) 213–218.
[3] Y. Zhang, T. Zuo, Z. Tang, et al., Prog. Mater. Sci. 61 (2014) 1–93.
[4] D.B. Miracle, O.N. Senkov, Acta Mater 122 (2017) 448–511.
[5] B. Cludovatz, A. Hohenwarter, D. Canoor, et al., Science 345 (2014) 1153–1158.
[6] W. Zhang, A. Chabok, B.J. Kooi, et al., Mater. Des. 220 (2022), 110875.
[7] S. Zhu, D. Yan, K. Gan, et al., Scr. Mater. 191 (2021) 96–100.
[8] J. Su, X. Wu, D. Raabe, et al., Acta Mater 167 (2019) 23–39.
[9] J. Tu, K. Xu, Y. Liu, et al., Intermetallics 144 (2022), 107508.
[10] Z. Li, Acta Mater 164 (2019) 400–412.
[11] C. Haase, L.A. Barrales-Mora, Metals (Basel) 9 (7) (2019) 726.
[12] Z. Li, C. Tasan, H. Springer, et al., Sci. Rep. 7 (2017) 40704.
[13] G. Laplanche, A. Kostka, O.M. Horst, et al., Acta Mater 118 (2016) 152–163.
[14] S. Thapliyal, S.S. Nene, P. Agrawal, et al., Addit. Manuf. 36 (2020), 101455.
[15] Y.M. Wang, T. Voisin, J.T. McKeown, et al., Nat. Mater. 17 (1) (2018) 63–70.
[16] B. Dovgyy, A. Piglione, P.A. Hooper, et al., Mater. Des. 194 (2020), 108845.
[17] O.G. Nimaga, B.B. He, G.J. Cheng, et al., Int. J. Plast. 123 (2019) 165–177.
[18] Z.G. Zhu, X.H. An, W.J. Lu, et al., Mater. Res. Lett. 7 (11) (2019) 453–459.
[19] L. Lutterotti, D. Chateigner, S. Ferrari, et al., Thin Solid Films 450 (2004) 34–41.
[20] R. Maaß, M.D. Uchic, Acta Mater 60 (3) (2012) 1027–1037.
[21] J.M. Park, P. Asghari-Rad, A. Zargaran, et al., Acta Mater 221 (2021), 117426.
[22] D. Kong, C. Dong, S. Wei, et al., Addit. Manuf. 38 (2021), 101804.
[23] W. Kurz, C. Bezencon, M. Gäumann, Sci. Technol. Adv. Mat. 2 (2001) 185–191.
[24] S. Guan, D. Wan, K. Solberg, et al., Scr. Mater. 183 (2020) 133–138.
[25] D. Wei, X. Li, J. Jiang, et al., Scr. Mater. 165 (2019) 39–43.
[26] S. Kurosu, H. Matsumoto, A. Chiba, et al., Metall. Mater. Trans. A 41 (10) (2010) 2613–2625.
[27] W. Wu, R. Zhou, B. Wei, et al., Mater. Charact. 144 (2018) 605–610.
[28] R. Zhou, Y. Liu, B. Liu, et al., Intermetallics 106 (2019) 20–25.
[29] J.M. Park, E.S. Kim, H. Kwon, et al., Addit. Manuf. 47 (2021), 102283.
[30] J.M. Park, J. Choe, J.G. Kim, et al., Mater. Res. Lett. 8 (2019), 1638844.
[31] J.M. Park, J. Choe, H.K. Park, et al., Addit. Manuf. 35 (2020), 101333.
[32] J.G. Kim, J.M. Park, J.B. Seol, et al., Mater. Sci. Eng. A 773 (2020), 138726.
[33] Y.K. Kim, J.H. Yu, H.S. Kim, et al., Compos. Part B-Eng. 210 (2021), 108638.
[34] H. Chen, T. Lu, Y. Wang, et al., Mater. Sci. Eng. A 833 (2022), 142512.
[35] B. Li, L. Zhang, Y. Xu, et al., Powder Technol 360 (2020) 509–521.
[36] B. Li, L. Zhang, B. Yang, Compos. Commun. 19 (2020) 56–60.
[37] B. Li, B. Qian, Y. Xu, et al., Mater. Lett. 252 (2019) 88–91.
[38] M. Song, R. Zhou, J. Gu, et al., Appl. Mater. Today 18 (2020), 100498.
[39] R. Zhou, Y. Liu, C. Zhou, et al., Intermetallics 94 (2018) 165–171.
[40] Y. Koizumi, S. Suzuki, K. Yamanaka, et al., Acta Mater 61 (5) (2013) 1648–1661.
[41] P. Jacques, Q. Furnémont, A. Mertens, et al., Philos. Mag. A 81 (7) (2001) 1789–1812.
[42] Y. Zhu, X. Wu, Mater. Res. Lett. 7 (2019) 393–398.
[43] Y. Zhu, K. Ameyama, P.M. Anderson, et al., Mater. Res. Lett. 9 (2021) 1–31.
[44] S.T. Pisarik, D.C. Van Aken, Metall. Mater. Trans. A 45 (8) (2014) 3173–3178.
[45] L. Lu, X. Chen, X. Huang, et al., Science 323 (5914) (2009) 607–610.
[46] P. Wang, F. Liu, Y. Cui, et al., Int. J. Plast. 107 (2018) 150–163.
[47] J. Li, Q. Fang, B. Liu, et al., Acta Mater 147 (2018) 35–41.
[48] J.J. Roa, J.M. Wheeler, T. Trifonov, et al., Mater. Sci. Eng. A 647 (2015) 51–57.